Table of Contents

SUPPLEMENTARY FIGURES

Supplementary Figure 1. The effect of sequence context on CPD formation, CPD repair, and 6-4 PP formation

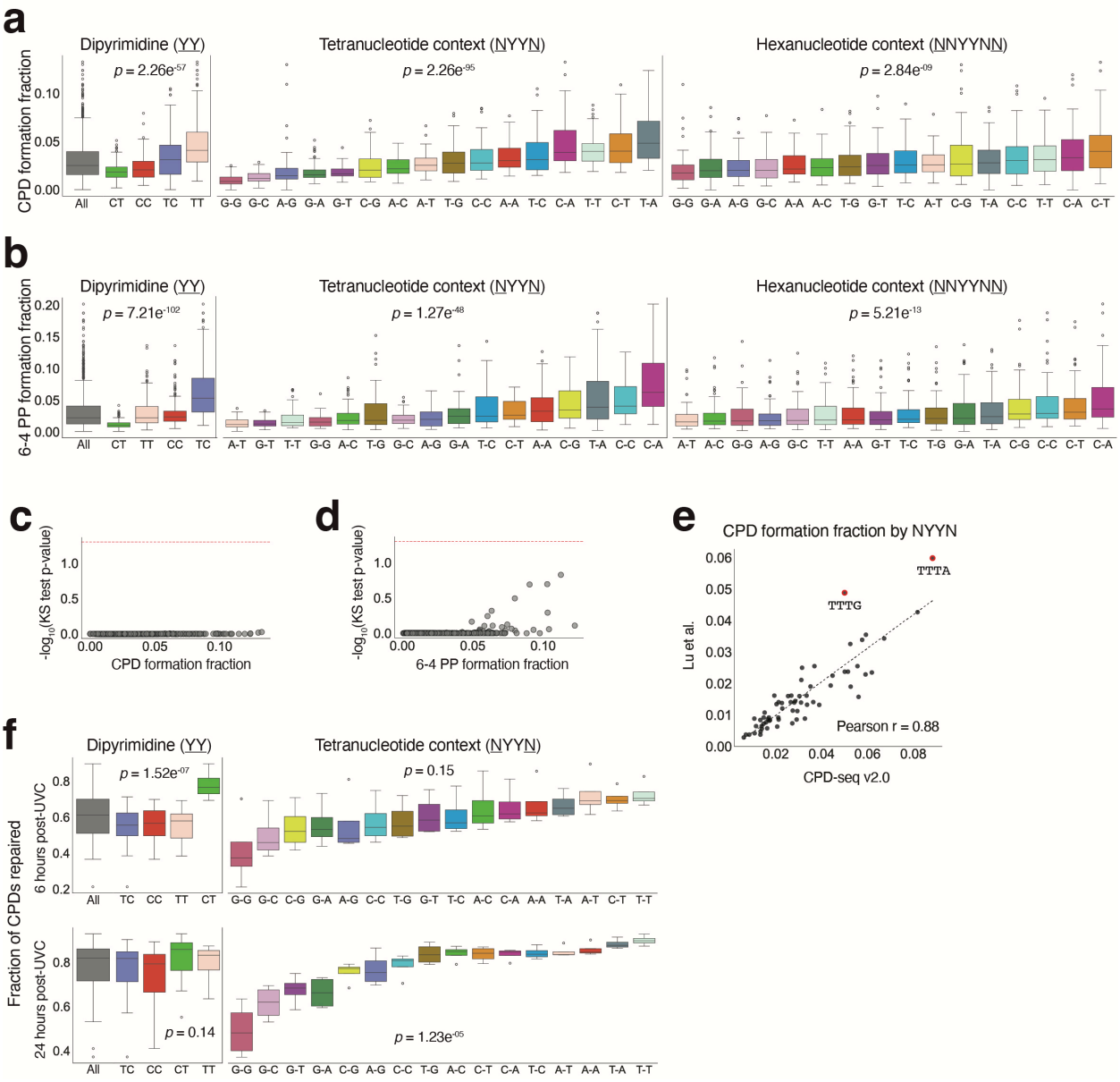

a Box plots of CPD formation fraction grouped by dipyrimidines, tetranucleotide (NYYN), and hexanucleotide (NNYYNN) sequence context. CPD counts were aggregated from CPD-seq v2.0 data[1] of all intergenic, chromatin accessible regions in human skin fibroblasts, processed immediately after irradiation with 6J/m² UVC. Y-axis defined as $CPDcount_k/count_k$, where k is the given k-mer sequence.

b As in panel a, but for 6-4 PP formation. Panels b and d include Kruskal-Wallis test p-values for each sequence context grouping.

c Scatter plot of $-log10$ transformed p-values computed from Kolmogorov-Smirnov (KS) tests comparing the theoretical Poisson and actual CPD formation count distribution for each NNYYNN sequence.

Distributions were derived from CPD-seq v2.0 data in the same genomic regions described in panel a. All datapoints are beneath the red dashed line (p=0.05), indicating that the theoretical Poisson distribution does not significantly deviate from the actual CPD data per the KS test for all NNYYNNs.

d As in panel c, but for 6-4 PP formation.

e Scatter plot showing correlation of NYYN sequence CPD formation frequencies derived from CPD-seq v2.0 *in vivo* data published by Duan et al. (x-axis) and in vitro frequencies (y-axis) reported by Lu and colleagues.[2] CPD-seq v2.0 data measurements were calculated from intergenic, open chromatin regions in human skin fibroblasts irradiated with 6J/m2 UVC. The dashed line is the ordinary least squares fit of the data. Overall, the two experiments are strongly correlated (Pearson r=0.88). Sequence TTTG is an outlier (OLS residual error p-value=1.3e-5), where the CPD formation frequency reported by Lu et al. is significantly discordant from the CPD-seq v2.0 derived frequencies. This discrepancy may be a reflection of the much higher UVC dosage used by Lu et al. (500J/m2 over 8 seconds vs. just 6J/m2 used by Duan et al.). Sustained exposure to high dosages of UVC is known to cause CPD photoreversal, especially for cytosine-containing NYYN sequences[2–4]. Thus, the formation frequency of sequences that are less susceptible resistant to photoreversibility,like TTTG, (and TTTA to a lesser extent), may appear disproportionately high due to the large UVC dosage condition used in Lu et al.

f Box plots of CPD repair efficiency grouped by YY and NYYN sequence context, calculated using CPD-seq v2.0 data in the same genomic regions described in **a** but from 6J/m^2 UV irradiated cells given 6 (top) and 24 (bottom) hours of repair. Y-axis defined as $1 - (6hr\ CPD\ count_k / 0hr\ CDP\ count_k)$ for a given k-mer, k. Included are Kruskal-Wallis test p-values for each sequence context grouping.

Supplementary Figure 2. Differential CPD formation in ETS and CTCF binding sites is a function of TF binding

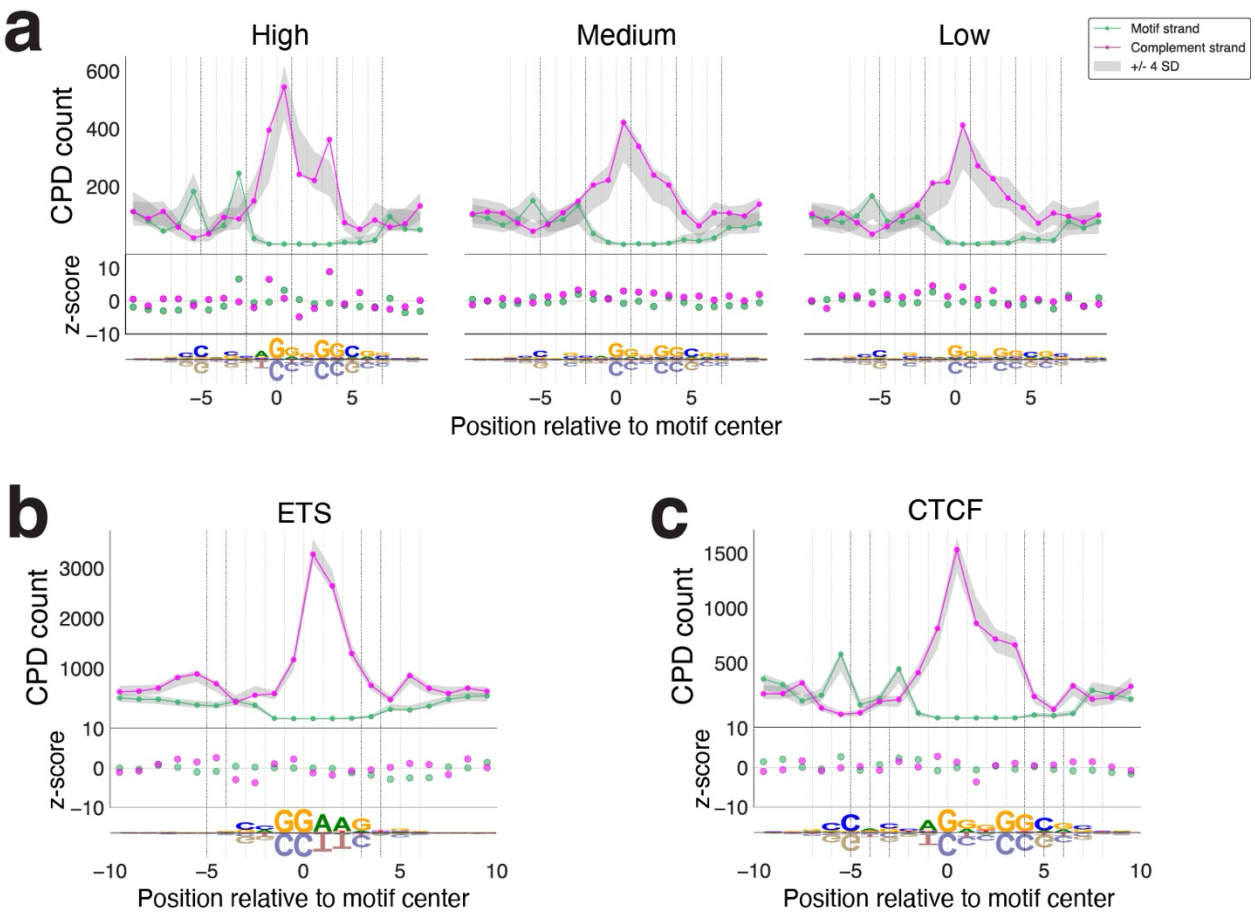

a Full analysis of CPD formation in active CTCF binding sites[5] (n=56,765), stratified by binding site strength. Binding sites were divided into equal thirds based on MOODS motif quality score[6], with higher scores indicating stronger CTCF binding. Green and pink lines CPD profile plot represent raw CPD counts per position on the CTCF motif and motif-complement strands, respectively. CPD marker positions are between nucleobase positions, indicating the photodimer location. Gray shaded region in the represents expected CPD levels +/-4 standard deviations, according to the background model of CPD formation, conditioned on the cumulative hexanucleotide sequence content at each position. Included below the CPD profiles are z-scores per position, colored by strand. Sequence logos show motif content of sites used in each binding strength tier. X-axis denotes position relative to the binding motif center.

b Similar to **a**, but for CPD formation analysis of high-affinity ETS binding sites (n=15,583) in naked DNA that was first extracted from human skin fibroblasts and purified of proteins before irradiation with 12J/m^2. See Duan et al. for details[1]. Background model was developed as described in the "Poisson modelling of CPD formation at TF binding sites" Methods section but using naked DNA CPD-seq v2.0 data.

c Equivalent to **b** but for CPD formation in high-affinity CTCF binding sites (n=28,384) in naked DNA.

Supplementary Figure 3. TF binding effects on CPD formation are consistent across analytical and simulation analysis methodologies

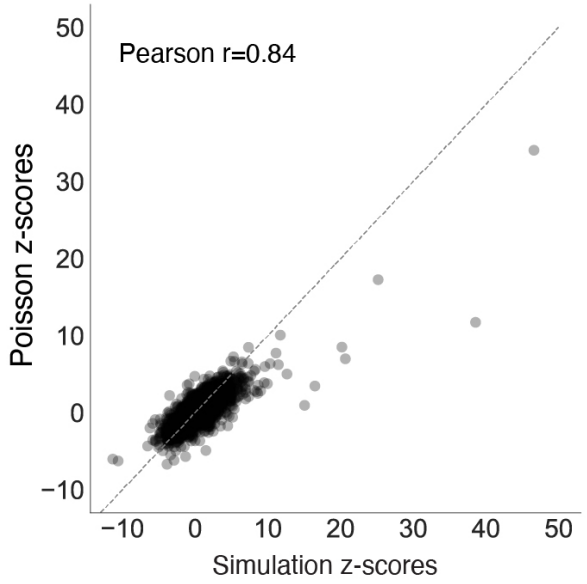

Scatter plot showing correlation between results of CPD formation analysis as evaluated by the simulation permutation testing method (x-axis) and analytical Poisson method (y-axis). Each marker is the z-score of an individual position in the TF binding site window across all 225 TF clusters included in the analysis. The permutation testing simulation was performed as described in the “Modulation of CPD formation and C>T transitions in TF binding sites using simulation” Supplementary Methods section. Poisson method is described in the “Poisson modelling of CPD formation at TF binding sites” Methods section.

Supplementary Figure 4. Dynamics of CPD repair modulation at active TF binding sites

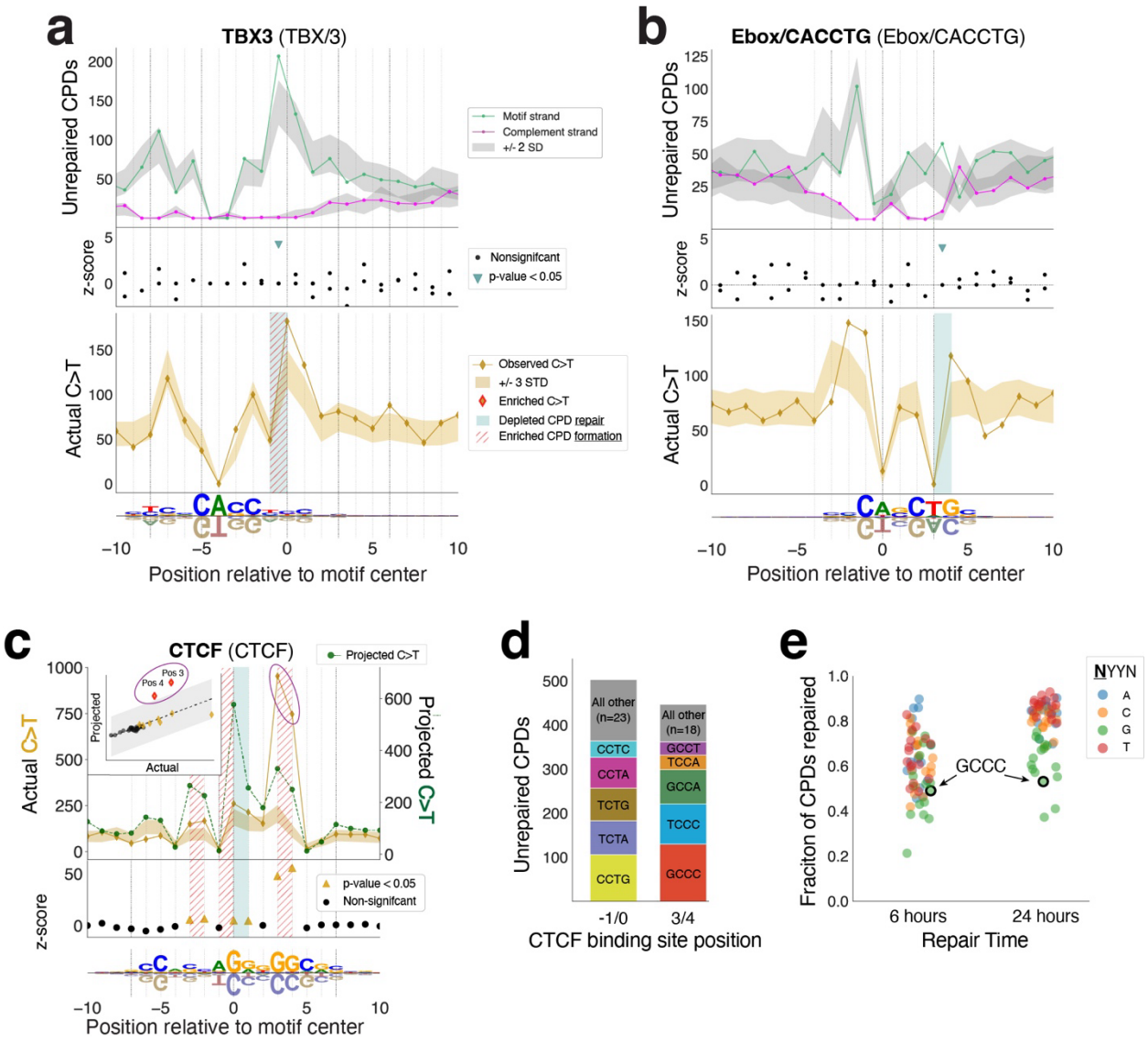

a Analysis of unrepaired CPDs in active TBX3 binding sites (n=9,844) 6h after irradiation with 6J/m². (Top) Gray shaded region is +/- 2 standard deviations according a simulation of unrepaired CPDs at 6h, conditioned on tetranucleotide sequence content and CPD formation burden at each position. (Middle) Scatter plot of z-scores calculated from bootstrapping analyses per position and strand. Significant repair depletion (p<.05, BH corrected) is denoted with triangle markers. (Bottom) C>T mutation analysis of TBX3 binding sites as in **Main Fig. 3**. Significant C>T enrichment (p<0.05, BH corrected) is highlighted with red diamonds, positions with repair depletion are shaded teal, and positions with enriched CPD formation are crosshatched red.

b Similar to a, but for active Ebox/CACCTG transcription factor binding sites (n=12143).

c Full comparative analysis of actual vs. projected C>T mutation profiles for CTCF. Dark green line shows the mutation counts projected from CPD counts immediately after UVC irradiation (right y-axis). Z-scores for the actual mutation counts, according to the background model of C>T mutation frequency, are shown for each position. Triangle gold markers denote positions with significantly enriched C>T mutation levels (p<0.05, BH corrected). Positions with vertical red shading indicate CPD formation enrichment. Inset shows

a direct comparison between the actual C>T mutation counts vs. the projected C>T mutation counts; each point is a position in the CTCF binding site. Gray shaded region is +/- 3 standard deviations from the ordinary least squares fit of the data (dashed line, **Methods**). Positions 3 and 4 are significantly discordant from the projected C>T CTCF profile and circled in both the inset and mutation profile (OLS residual error z-score > 2.58).

d Bar plots of tetranucleotide content of CPDs formed immediately after 6J/m^2 UVC irradiation at positions -1/0 and 3/4 on the motif-complement strand of CTCF binding sites.

e Strip plots showing the fraction of CPDs repaired for all 64 NYYN at 6 and 24 hours, where each marker is a unique tetranucleotide colored by their 5' nucleobase. GCCC is annotated.

Supplementary Figure 5. General base substitution mutation enrichment in NFY binding site flanks

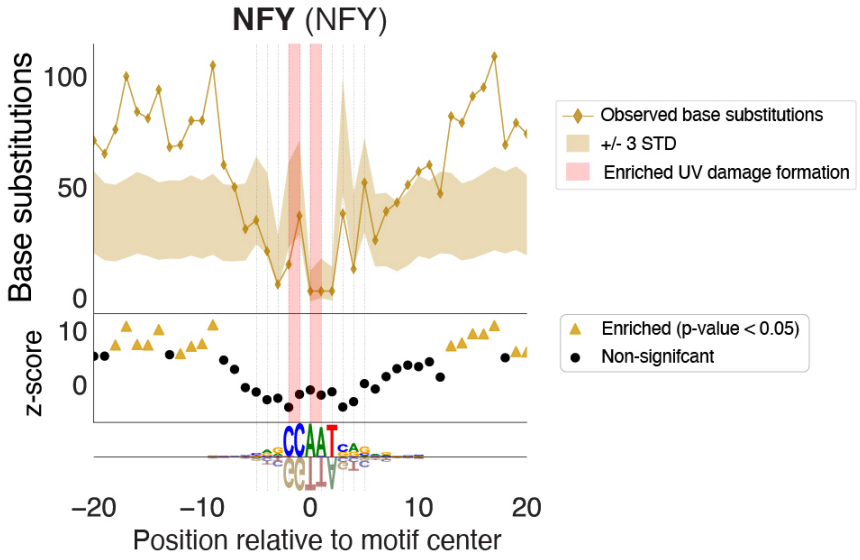

Analysis of all base substitution mutations in active NFY binding sites (n=4,195). Mutations were aggregated across both DNA strands for a total mutation count per TF binding site position. Shaded gold region denotes +/-3 standard deviations for expected mutation counts according to an analytical background model of mutation frequency across all base substitution types (**Methods**). UV damage formation hotspot positions identified in our prior analyses are shaded red, where motif position -2/-1 was enriched for 6-4 PPs (z-score=42.69) and motif-complement position 0/1 was enriched for CPDs (z-score=11.21) immediately UV irradiation.

Supplementary Figure 6. Structural analysis of TF-bound dipyrimidines using AlphaFold 3

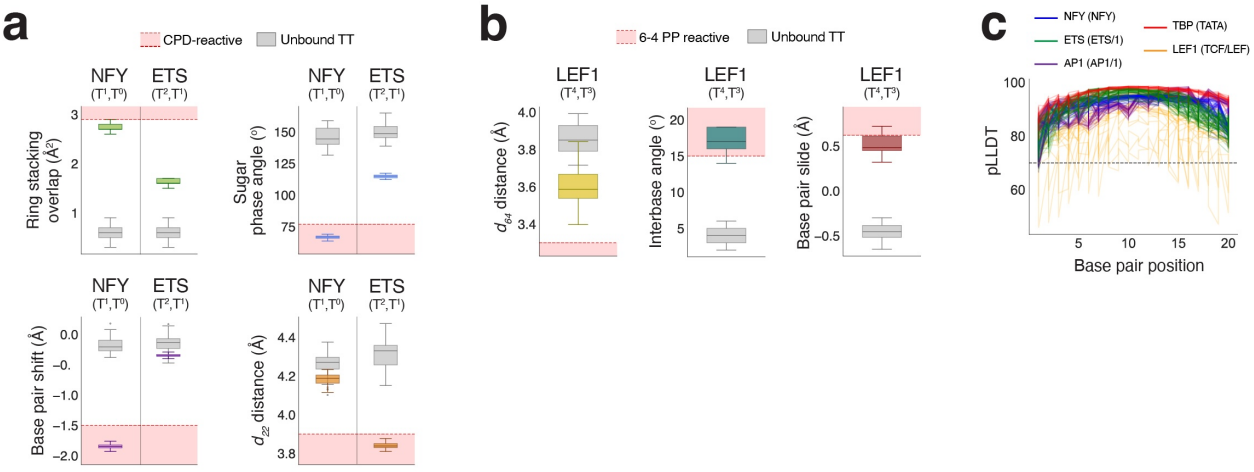

a As a control against NFY T^1T^0 (z-score=11.21), we performed a structural analysis (as described in "Structural analysis of AlphaFold 3 (AF3) predicted TF-DNA complexes" Methods section) for position 1/2 on the motif-complement strand of ETS binding sites, which also has a conserved TT but does not have significant CPD formation enrichment (z-score=1.60). Shown are boxplots of CPD-relevant structural parameters for ETS T^2T^1 across 20 ETS binding sites (TF motif cluster: ETS/1) when bound by ETS (colored box plots) versus unbound (gray boxplots). Red shaded regions signify the CPD-reactivity thresholds characteristic of TT photodimer formation in unbound, duplexed DNA previously reported[7]. While ETS T^2T^1 in the TF-bound state shows a slight increase in base stacking, the average ring stacking overlap, base pair shift, and sugar phase angle remain well outside the thresholds for TT CPD photoreactivity. Interestingly, the ETS T^2T^1 does have a shortened d_{22} distance that falls in the CPD photoreactive range. This short C_5-C_6 interbond distance, in the absence of the necessary base stacking, does not appear to be sufficient for CPD formation enrichment.

b Equivalent analysis to **a** but for 6-4 PP-relevant structural parameters for T^4T^3 on the motif-complement strand of 20 LEF1 binding sites (TF motif cluster: TCF/LEF) which we found to be enriched for 6-4 PP formation (z-score=10.05).

c Line plots of average predicted local distance test (pLDDT) scores per DNA residue position for AF3 structural predictions of NFY, ETS, AP1, TBP, and LEF1 binding sites, bound by their putative TF. The pLDDT score was averaged across each DNA residue for the top-ranking structural prediction per AF3 run. The "confident" pLDDT threshold (pLDDT>=70), per AF3 documentation[8], is shown as a dashed line.

Supplementary Figure 7. Bootstrap modelling of CPD repair in TF binding sites using timecourse data

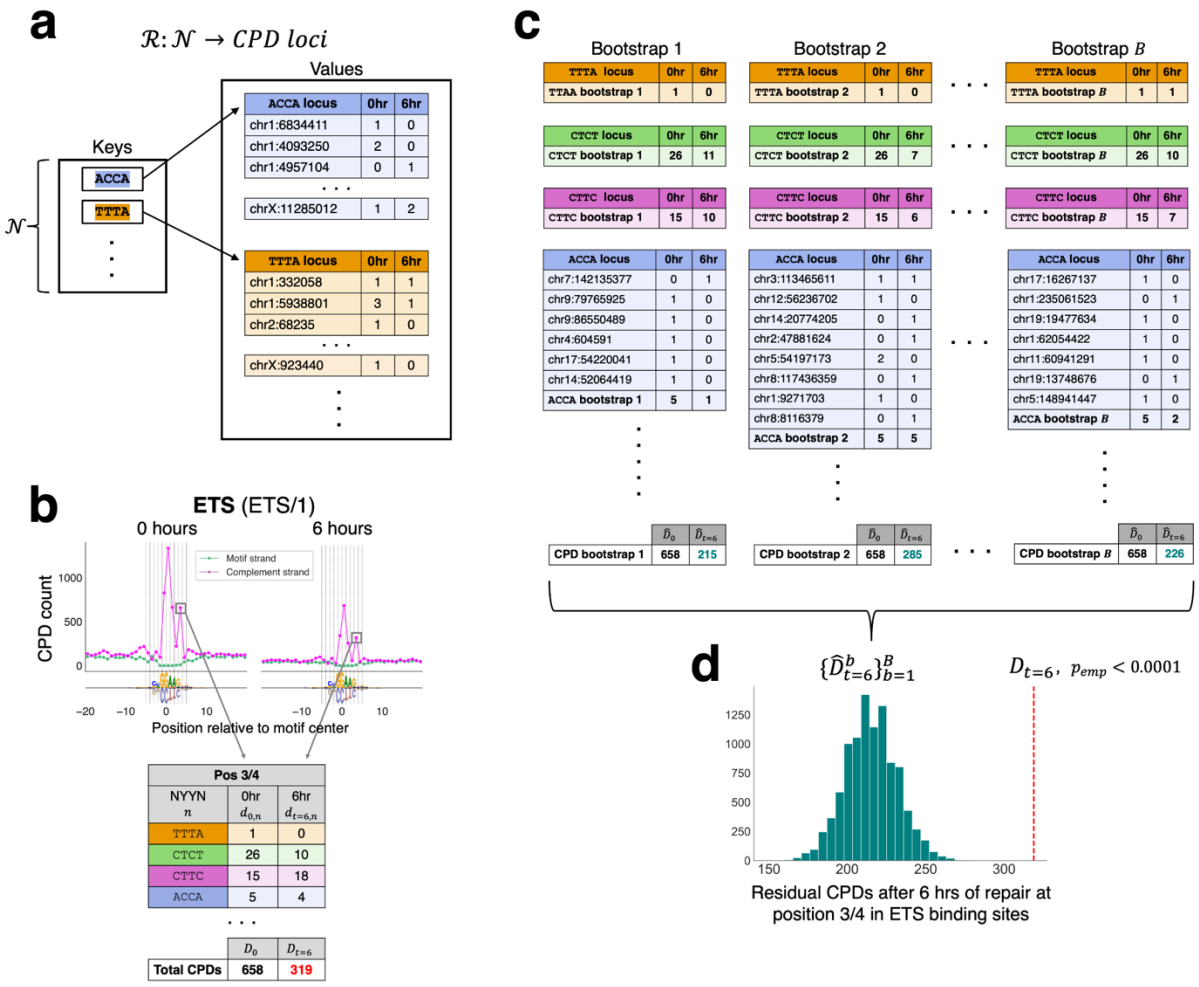

Accompanying figure to the "Simulation of CPD repair in TF binding sites" Supplementary Methods section.

a Repair dictionary where all UV-damageable tetranucleotides (NYYN) are mapped to intergenic, open-chromatin CPD-seq v2.0 data from two repair timepoints and then merged on genomic locus. Each NYYN dictionary value consists of a dataframe where each row is a CPD genomic locus, where each locus has two columns containing the corresponding CPD counts at 0 and 6 hours. Genomic loci that were undamaged in both timepoints are superfluous to the analysis and therefore not included.

b CPD profiles of aggregated ETS binding sites (TF motif cluster: ETS/1) immediately after (e.g. 0hrs, left) and 6 hours (right) after irradiation with 6J/m^2 UVC. Below is an example of the CPD sequence composition at position 3/4 on the motif-complement strand for both repair timepoints with the total CPD damage adding up to 658 and 319 for both 0 and 6 hours, respectively. The CPD counts at 0 hours we refer to as the *CPD formation burden*.

c Schematic of bootstrapping strategy as described in the Supplementary Methods. For each NYYN, the repair dictionary is randomly sampled with replacement to predict the residual CPD counts after 6 hours of repair, such that the sampled CPD formation burden equals the observed CPD formation burden. The predicted residual CPD counts are summed across all NYYN to obtain the total predicted CPD level after 6 hours of repair. This bootstrap sampling is repeated many times to generate an empirical distribution to compare against observed CPD levels at 6 hours for hypothesis testing.

d Histogram of bootstrapped (B=10,000) residual CPD counts at ETS motif-complement position 3/4 after 6 hours of repair time. Our analysis shows that we observe significantly higher CPD levels (n=319) than the null distribution at 6 hours, indicating that CPDs are repaired less efficiently when they form at this binding site position.

SUPPLEMENTARY TABLES

Table 1. List of TFs included in the study

Full list of TF motif clusters and TF proteins used in study.

Table 2. CPD formation, CPD repair efficiency, and 6-4 PP formation by sequence context

CPD and 6-4 PP formation frequencies and CPD repair efficiencies by DNA sequence context. Measurements derived from chromatin accessible, intergenic regions of UV irradiated human skin fibroblasts that were used for model development.

Table 3. TF effects on CPD formation, CPD repair, 6-4 PP formation

CPD formation, 6-4 PP formation, and CPD repair analyses results for all TF motif clusters studied.

Table 4. Analysis results for C>T mutations in skin cancer samples

C>T mutation analysis results for all TF motif clusters studied.

Table 5. Input to AlphaFold 3 experiments and structural measurements

Full list of TF binding sites sequences and TF protein sequences used in AlphaFold3 runs and complete structural measurements.

Table 6. ATAC-seq QC summary

Run summary, metadata, and QC results of ATAC-seq experiment of C1SAN/CSB^{WT} cells.

Table 7. Multiple linear regression of tetranucleotide sequence features on CPD repair efficiency

		Coefficient	*β (SE)*	*t*	*p-value*
6 hrs of repair R^2=0.869 Adj. R^2=0.847	Intercept	0.630217	0.021194	29.736010	3.701761e-35
	YY: CT	0.219292	0.018956	11.568353	3.072142e-16
	5': G	-0.130028	0.018956	-6.859391	6.969866e-09
	3': G	-0.114892	0.018956	-6.060921	1.361651e-07
	3': C	-0.054716	0.018956	-2.886459	5.590889e-03
	3': T	0.052153	0.018956	2.751253	8.064044e-03
	5': C	-0.032108	0.018956	-1.693821	9.606070e-02
	YY: TC	-0.014730	0.018956	-0.777041	4.405256e-01
	5': T	-0.006274	0.018956	-0.330962	7.419542e-01
	YY: TT	-0.001696	0.018956	-0.089444	9.290597e-01
24 hrs of repair R^2=0.877 Adj. R^2=0.857	Intercept	0.814320	0.017898	45.497084	9.564602e-45
	5': G	-0.216666	0.016009	-13.534284	5.435694e-19
	3': G	-0.096880	0.016009	-6.051716	1.408788e-07
	YY: CT	0.083589	0.016009	5.221484	2.911058e-06
	YY: TT	0.071993	0.016009	4.497113	3.691986e-05
	3': C	-0.038298	0.016009	-2.392330	2.025131e-02
	5': T	0.037196	0.016009	2.323477	2.394812e-02
	YY: TC	0.031564	0.016009	1.971662	5.378042e-02
	5': C	-0.024556	0.016009	-1.533908	1.308908e-01
	3': T	0.004867	0.016009	0.304046	7.622615e-01

Multiple ordinary least squares (OLS) regression analysis was performed using the Python statsmodel.formula.api OLS implementation (v0.14.0). Regression was used to assess tetranucleotide (NYYN) sequence features as predictors of repair efficiency in 6J/m^2 UVC irradiated human skin fibroblasts after 6 and 24 hours of repair. Repair efficiency (i.e. fraction of CPDs repaired) was defined as $1 - (0hr\ CPD\ count/Xhr\ CPD\ count)$ and derived from all intergenic, open chromatin regions to isolate effects of GG-NER. We note that our results agree with previous studies analyzing sequence specificity of CPD excision using XR-seq data[9,10], with earlier repair (within 6 hours) being highly biased towards CT dipyrimidines, while consistent across both timepoints, dipyrimidines flanked by guanines were repaired significantly slower.

SUPPLEMENTARY METHODS AND MATERIALS

Simulation of CPD repair in TF binding sites

CPD-seq v2.0 timecourse data of human skin fibroblast cells given 0 or 6 hours of repair time after irradiation with 6J/m^2 UVC was used to analyze CPD repair in aggregated TF binding sites using bootstrap sampling. In **Supplementary Fig. 1c** and **Supplementary Table 7**, we see that dipyrimidine type and tetranucleotide sequence context significantly impacts CPD repair efficiency. Because we are interested in the repair trends of aggregated damage in TF binding sites per position, it is important to consider the relationship between repair efficiency and the amount of cumulative CPD damage formed immediately after irradiation.

CPD formation is a rare, stochastic event such that the damage landscape between CPD-seq experiments is heterogeneous. This means that the same genomic locus between two independent CPD experiments will rarely form a CPD in both cases. While this heterogeneity is theoretically unbiased when estimating CPD repair efficiency when there is a sufficient starting amount of CPDs, as the number of initial CPDs decreases, the signal-to-noise ratio also diminishes, limiting statistical assessment of repair.

Thus, in our analysis of repair efficiency, we consider the residual CPD count, D_t at a given aggregated TF binding site position after a defined repair interval, t, to be dependent on both sequence composition and the CPD damage formation burden immediately after irradiation, D_0.

To serve as a null distribution, we created a synthetic dataset in the form of a repair dictionary, $\mathcal{R}$, where all UV-damageable tetranucleotides (NYYN) are mapped to CPD-seq v2.0 data from two repair timepoints and then merged on genomic locus (**Supplementary Fig. 7a**). The data in $\mathcal{R}$ is derived from intergenic, open chromatin regions to best capture cis-regulatory regions that we assume are the primary binding targets for TFs[11], focusing our analysis on GG-NER mechanisms and excluding TC-NER activity that is mostly active in genic introns and exons[12].

Let p be a position in TF's aggregated binding sites and $\mathcal{N} = \{NYYN\}$ represent the set of all 64 UV-damageable tetranucleotide sequences.

The total initial CPD formation burden at p, is distributed across $\mathcal{N}$ in varying proportions (**Supplementary Fig. 7b**).

For each sequence $n \in \mathcal{N}$, at position p, define the observed CPD formation burden as $d_{0,n}$.

To simulate repair, we randomly sampled $\mathcal{R}(n)$ with replacement such that,

$$\hat{d}_{0,n} = d_{0,n}$$

where $\hat{d}_{0,n}$ is the sampled CPD formation burden from $\mathcal{R}(n)$ (**Supplementary Fig. 7c**).

Because $\mathcal{R}$ contains genomic loci with paired CPD counts measured at timepoints 0 and t, each sampling is accompanied by the corresponding residual CPD counts for n given repair time t, denoted as $\hat{d}_{t,n}$.

To determine the total predicted CPD damage at p after t hours of repair, we sum $\hat{d}_{t,n}$ across $\mathcal{N}$:

$$\widehat{D}_t = \sum_{n \in \mathcal{N}} \hat{d}_{t,n}$$

We repeat this process for $B = 10{,}000$ bootstrap samples to create an empirical distribution, $\{\widehat{D}_t^b\}_{b=1}^B$ of total residual CPDs at p given repair t (**Supplementary Fig. 7d**).

Using this empirical distribution as our null, we then perform hypothesis testing at p, to assess if the observed residual CPD signal is smaller than expected. Such that for samples in $\{\widehat{D}_t^b\}_{b=1}^B$,

$$H_0: D_t \leq \widehat{D}_t^b, \text{ and}$$

$$H_A: D_t > \widehat{D}_t^b$$

We calculate a one-sided empirical p-value as follows:

$$P_{emp} = \frac{1}{B} \sum_{b=1}^{B} I\left[\widehat{D}_t^b \geq D_t\right].$$

If the $P_{emp} < 0.05$ (after BH correction), we reject the null hypothesis and say that the observed residual CPD signal at p is significantly higher than expected after t repair time, indicating that CPDs are repaired less efficiently when they form at p. We infer that such effects are the result of TFs stills successfully complexing with their binding sites even when these affected positions are dimerized as a CPDs, thus competing with repair factors for UV lesion recognition and attenuating the repair process.

Modulation of CPD formation and C>T transitions in TF binding sites using simulation

We used a simulation-based method to quantify the significance and magnitude of CPD and C>T mutation enrichment and depletion patterns at each position in the TF binding site windows of the 225 TF motif clusters we curated for the study. This procedure involves a two-step process. First, CPD and C>T counts across intergenic, accessible chromatin regions were extracted, and aggregated by immediate sequence (NYYN for CPDs, and the (NYN for mutations). Then, the total counts observed at each sequence were redistributed uniformly across all positions matching that sequence (or its reverse complement) within the targeted region. This approach preserves the original global damage and mutation counts for each sequence context through multinomial randomization (numpy.random.multinomial), while randomizing the specific genomic locations of these events. This redistribution was performed 10,000 times to model the background CPD and mutation distributions based solely on sequence context.

To evaluate the TF-binding effects on CPD formation and C>T enrichment, we intersected active TF binding site windows (here, defined as +/- 20 base pairs relative to the center of the TF cluster binding motif) with actual counts and then again with simulated counts to create a per-position null distributions for CPD formation and C>T enrichment, respectively. Then, the expected counts from the background model were scaled to match the mean frequencies of CPDs or C>Ts in the flanks (defined as further than five base pairs outside of the motif). This scaling was done separately for each strand (both counts on the motif and complement strand) and each half of the TF motif. We then calculated one-sided empirical p-values to quantify the statistical significance

of both enrichment and depletion at each position; the p-value for enrichment was calculated as the proportion of simulated counts (post-adjustment; out of 10,000) that exceeded the observed count at that position, and the p-value for depletion was calculated as the proportion of simulated counts that were less than the observed count. BH p-value multiple test correction was then applied across all positions in the TF binding site window. Additionally, we calculated the mean and standard deviation of the simulated null distribution at each position for z-scores, allowing us to compare the magnitudes of enrichment or depletion effects at each position.

UVDE-seq oligos and adaptors

Oligos for first adapter ligation:

trP1-top (5′-CCTCTCTATGGGCAGTCGGTGAT-phosphorothioate-T-3′)

trP1-bottom (5′-phosphate-ATCACCGACTGCCCATAGAGAGGC-dideoxy-3′).

Oligos for second adapter ligation:

A1-top (5′-phosphate-ATCCTCTTCTGAGTCGGAGACACGCAGGGATGAGATGGCdideoxy-3′), A1-bottom (5′-biotin-CCATCTCATCCCTGCGTGTCTCCGACTCAGAAGAGGATNNNNNN-C3 phosphoramidite-3′);

A2-top (5′-phosphate-ATCACGAACTGAGTCGGAGACACGCAGGGATGAGATGGCdideoxy-3′), A2-bottom (5′-biotin-CCATCTCATCCCTGCGTGTCTCCGACTCAGTTCGTGATNNNNNN-C3 phosphoramidite-3′);

A3-top (5′-phosphate-ATCTCAGGCTGAGTCGGAGACACGCAGGGATGAGATGGCdideoxy-3′), A3-bottom (5′-biotin-CCATCTCATCCCTGCGTGTCTCCGACTCAGCCTGAGATNNNNNN-C3 phosphoramidite-3′).

A4-top (5’-phosphate-ATCGCGATCTGAGTCGGAGACACGCAGGGATGAGATGGCdideoxy-3’); A4-bottom (5’- biotin-CCATCTCATCCCTGCGTGTCTCCGACTCAGATCGCGATNNNNNN-C3 phosphoramidite-3’);

A5-top (5′- phosphate-ATCCAGTACTGAGTCGGAGACACGCAGGGATGAGATGGCdideoxy-3′); A5-bottom (5′- biotin-CCATCTCATCCCTGCGTGTCTCCGACTCAGTACTGGATNNNNNN-C3 phosphoramidite-3′)

A6-top (5′- phosphate-ATCAGTTCCTGAGTCGGAGACACGCAGGGATGAGATGGCdideoxy-3′); A6-bottom (5′- biotin-CCATCTCATCCCTGCGTGTCTCCGACTCAGGAACTGATNNNNNN-C3 phosphoramidite-3′)

Oligonucleotides used for PCR confirmation and library amplification:

Primer A (5′-CCATCTCATCCCTGCGTGTCTCCGAC-3′)

Primer trP1 (5′-CCTCTCTATGGGCAGTCGGTGATT-3′).

SUPPLEMENTARY REFERENCES

1. Duan, M. *et al.* High UV damage and low repair, but not cytosine deamination, stimulate mutation hotspots at ETS binding sites in melanoma. *Proceedings of the National Academy of Sciences* **121**, e2310854121 (2024).

2. Lu, C., Gutierrez-Bayona, N. E. & Taylor, J.-S. The effect of flanking bases on direct and triplet sensitized cyclobutane pyrimidine dimer formation in DNA depends on the dipyrimidine, wavelength and the photosensitizer. *Nucleic Acids Research* **49**, 4266–4280 (2021).

3. Law, Y. K., Forties, R. A., Liu, X., Poirier, M. G. & Kohler, B. Sequence-dependent thymine dimer formation and photoreversal rates in double-stranded DNA. *Photochemical & Photobiological Sciences* **12**, 1431–1439 (2013).

4. Pan, Z., Chen, J., Schreier, W. J., Kohler, B. & Lewis, F. D. Thymine Dimer Photoreversal in Purine-Containing Trinucleotides. *J. Phys. Chem. B* **116**, 698–704 (2012).

5. Vierstra, J. *et al.* Global reference mapping of human transcription factor footprints. *Nature* **583**, 729–736 (2020).

6. Korhonen, J., Martinmäki, P., Pizzi, C., Rastas, P. & Ukkonen, E. MOODS: fast search for position weight matrix matches in DNA sequences. *Bioinformatics* **25**, 3181–3182 (2009).

7. Conti, I. *et al.* Multiple Electronic and Structural Factors Control Cyclobutane Pyrimidine Dimer and 6–4 Thymine–Thymine Photodimerization in a DNA Duplex. *Chemistry – A European Journal* **23**, 15177–15188 (2017).

8. Abramson, J. *et al.* Accurate structure prediction of biomolecular interactions with AlphaFold 3. *Nature* **630**, 493–500 (2024).

9. Hu, J., Adar, S., Selby, C. P., Lieb, J. D. & Sancar, A. Genome-wide analysis of human global and transcription-coupled excision repair of UV damage at single-nucleotide resolution. *Genes & development* **29**, 948–960 (2015).

10. Morledge-Hampton, B., Kalyanaraman, A. & Wyrick, J. J. Analysis of cytosine deamination events in excision repair sequencing reads reveals mechanisms of incision site selection in NER. *Nucleic Acids Research* **52**, 1720–1735 (2024).

11. Panigrahi, A. & O'Malley, B. W. Mechanisms of enhancer action: the known and the unknown. *Genome Biology* **22**, 108 (2021).

12. Fousteri, M. & Mullenders, L. H. Transcription-coupled nucleotide excision repair in mammalian cells: molecular mechanisms and biological effects. *Cell Research* **18**, 73–84 (2008).